PNAS
www.pnas.org

Main Manuscript for

Imaging active site chemistry and protonation states: NMR crystallography of the tryptophan synthase α-aminoacrylate intermediate

Jacob B. Holmes,[a,1] Viktoriia Liu,[a,1] Bethany G. Caulkins,[a,b,1] Eduardo Hilario,[a] Rittik K. Ghosh,[c] Victoria N. Drago,[d] Robert P. Young,[e] Jennifer A. Romero,[a] Adam D. Gill,[c] Paul M. Bogie,[a] Joana Paulino,[f] Xiaoling Wang,[f] Gwladys Riviere,[g] Yuliana K. Bosken,[c] Jochem Struppe,[h] Alia Hassan,[i] Jevgeni Guidoulianov,[i] Barbara Perrone,[i] Frederic Mentink-Vigier,[f] Chia-en A. Chang,[a] Joanna R. Long,[g] Richard J. Hooley,[a,c] Timothy C. Mueser,[d] Michael F. Dunn,[c,*] Leonard J. Mueller [a,*]

[1]co-first authors

a Department of Chemistry, University of California Riverside, Riverside, CA, 92521, USA
b Current address: W.M. Keck Science Department, Claremont McKenna, Pitzer and Scripps Colleges, Claremont, CA, USA
c Department of Biochemistry, University of California Riverside, Riverside, CA, 92521, USA
d Department of Chemistry and Biochemistry, University of Toledo, Toledo, Ohio 43606
e Environmental Molecular Sciences Laboratory, PNNL, Richland, WA 99354, USA
f National High Magnetic Field Laboratory, Florida State University, Tallahassee, FL, 32310, USA
g Department of Biochemistry and Molecular Biology, McKnight Brain, Institute and National High Magnetic Field Laboratory, University of Florida, Gainesville, FL, 32610-0245, USA
h Bruker Biospin Corporation, 15 Fortune Drive, Billerica, MA, United States
i Bruker Switzerland AG, Fällanden, Switzerland

Corresponding authors: Leonard J. Mueller, leonard.mueller@ucr.edu; Michael F. Dunn, michael.dunn@ucr.edu

Author Contributions:
Designed research: LJM, MFD. Performed research: JBH, VL, BGC, EH, RKG, VND, RPY, JAR, JP, XW, GR, YKB, JS, AH, JG, BP, FMV. Contributed new reagents/analytic tools: ADG, PMB, RJH. Analyzed data: LJM, MFD, TCM, RJH, JRL, CAC. Wrote paper: LJM, MFD, JBH, VL, BGC, RKG

Competing Interest Statement: The authors declare that they have no known competing financial interests.

Classification: Biological Sciences: Biophysics and Computational Biology

Data Availability: All new crystal structures reported in this work have been deposited with the Protein Data Bank. All NMR chemical shift data are reported in the article and/or Supplementary Information. Coordinates for the refined active sites are provided as part of the Supplementary Materials.

This PDF file includes:

Abstract (250 words max)

NMR-assisted crystallography – the integrated application of solid-state NMR, X-ray crystallography, and first-principles computational chemistry – holds significant promise for mechanistic enzymology. By providing atomic-resolution characterization of stable intermediates in enzyme active sites, including hydrogen atom locations and tautomeric equilibria, NMR crystallography offers insight into both structure and chemical dynamics. Here, this integrated approach is used to characterize the tryptophan synthase α-aminoacrylate intermediate, a defining species for pyridoxal-5′-phosphate-dependent enzymes that catalyze β-elimination and replacement reactions. For this intermediate, NMR-assisted crystallography is able to identify the protonation states of the ionizable sites on the cofactor, substrate, and catalytic side chains, as well as the location and orientation of crystallographic waters within the active site. Most notable is the water molecule immediately adjacent to the substrate β-carbon, which serves as a hydrogen bond donor to the ε-amino group of the acid-base catalytic residue, βLys87. From these, a detailed three-dimensional picture of structure and reactivity emerges, highlighting the fate of the L-serine hydroxyl leaving group and the reaction pathway back to the preceding transition state. Reaction of the α-aminoacrylate intermediate with benzimidazole, an isostere of the natural substrate, indole, shows benzimidazole bound in the active site and poised for, but unable to initiate, the subsequent bond formation step. When modeled into the benzimidazole position, indole is positioned with C3 in contact with the α-aminoacrylate C^{β} and aligned for nucleophilic attack. Here, the chemically-detailed, three-dimensional structure from NMR-assisted crystallography is key to understanding why benzimidazole does not react, while indole does.

Significance Statement (120 words max)

The determination of active site protonation states is critical for a full mechanistic understanding of enzymatic transformations. Yet hydrogen atom positions are challenging to extract using the standard tools of structural biology. Here we make use of a joint solid-state NMR, X-ray crystallography, and first-principles computational approach that enables the investigation of enzyme catalysis at this fine level of chemical detail. For tryptophan synthase, this allows us to peer along the reaction coordinates into and out of the α-aminoacrylate intermediate. Through this process, we are developing a high-resolution probe for structural biology that is keenly sensitive to hydrogen atom positions – complementing diffraction methods, yet able to be applied under conditions of active catalysis in microcrystalline and non-crystalline materials.

Introduction

Pyridoxal-5′-phosphate (PLP; Fig. 1) participates in numerous enzyme catalyzed reactions essential for amino acid metabolism, including transamination, decarboxylation, and α/β/γ-elimination and substitution (6-9). The power of PLP as a cofactor comes from its ability to act as an electron sink, allowing for the stabilization of carbanionic intermediates. A more subtle aspect of PLP chemistry demonstrated in β-elimination and replacement reactions is the ability of the cofactor to fine tune the polarity at the β-carbon of amino acids, facilitating the elimination of poor leaving groups and their replacement with weak nucleophiles.

Tryptophan synthase (TS) is the prototypical example of a PLP-dependent enzyme that catalyzes β-elimination and substitution. The *Salmonella typhimurium* tryptophan synthase (*St*TS) studied here is a 143 kDa αββα bienzyme complex (10). TS performs the final two steps in the biosynthesis of L-tryptophan: the α-subunit cleaves indole-3-glycerol 3′-phosphate (IGP) to glyceraldehyde-3-phosphate (G3P) and indole, while the β-subunit catalyzes the PLP-dependent β-elimination and replacement of the L-Ser hydroxyl with indole to produce L-Trp (Fig. 1) (11, 12). The fidelity of the proton transfers in the TS catalytic cycle are critical for maintaining the β-elimination and substitution pathway. In addition to the stereoelectronic control of the initial bond breaking step (13), it has been proposed that reaction specificity in PLP-dependent enzymes is modulated by the protonation states of the PLP cofactor-substrate complex (7, 9, 14), which are in turn directed by chemical interactions with acid-base groups such as βLys87 and βGlu109 in TS. Hence, the catalytic residues interacting with the cofactor establish the appropriate chemical and electrostatic environment to favor a particular protonation state and reaction pathway.

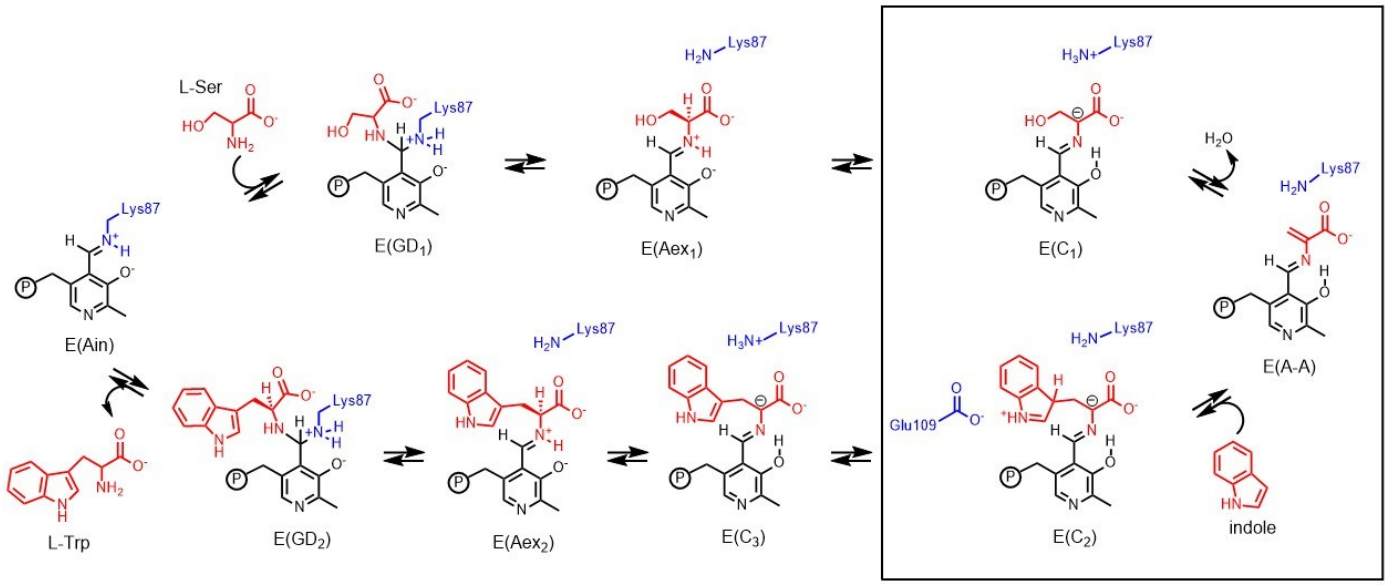

Fig. 1. TS β-site reaction, highlighting the α-aminoacrylate intermediate (1, 2). The PLP cofactor is drawn in black. In stage I of the reaction, L-Ser reacts with the internal aldimine, E(Ain), to give the gem-diamine, E(GD_1), and external aldimine, E(Aex_1), intermediates. Subsequent proton abstraction via βLys87 leads to the first carbanionic intermediate, E(C_1), and elimination of the β-hydroxyl group as water gives the α-aminoacrylate intermediate, E(A-A). In stage II, indole makes a nucleophilic attack at C^{β} of E(A-A) to yield a new C-C bond and the L-Trp carbanionic intermediate, E(C_2), and, upon deprotonation, E(C_3). In the final stages, E(C_3) is reprotonated, leading to the eventual release of L-Trp and the regeneration of E(Ain).

The determination of protonation states remains a significant challenge to the tools of structural biology. Even high-resolution X-ray crystal structures are challenged to place hydrogen atoms. Neutron crystallography can locate hydrogen atoms, offering remarkable insights into enzyme mechanism (15, 16). But the requirements for neutron crystallography include large, preferably perdeuterated crystals and multi-week-long acquisition times at room temperature. The latter currently precludes analysis of reactive intermediates such as those studied here. Cryo-EM is also pushing to the boundaries of resolution necessary for hydrogen atom detection (17), an extraordinary achievement, yet currently far from routine. In combined application with NMR spectroscopy, however, cryo-EM and diffraction methods continue to push toward complete, atomic-resolution descriptions of structure and function (18-30). For delineating the chemistry of the active site, NMR and diffraction become even more powerful when combined with first-principles computational chemistry (31-37).

We are developing NMR-assisted crystallography – the joint application of solid-state NMR (SSNMR), X-ray crystallography, and first-principles computational chemistry – to solve for the chemically-rich, three-dimensional structures of enzyme active sites (32-34). By "chemically-rich" we mean structures where the location of all atoms, including hydrogens, are specified. NMR crystallography was originally developed within the context of molecular organic and inorganic solids (38-44). Our group (32-34) and others (31, 35-37) have been working to extend this approach to structural biology, where it can provide consistent and testable models of enzyme structure and function. Our approach is three-fold. First, X-ray crystallography is used to provide a structural framework for the active site. Second, computational chemistry is used to build chemically-detailed models on this framework, and various active site chemistries are explored. Third, these models are quantitatively distinguished by comparing their predicted NMR chemical shifts to the results of solid-state NMR experiments. Provided that a sufficient number of chemical shifts are measured, NMR-assisted crystallography can identify a unique, consistent structure or, equally important, determine that none of the candidates is consistent with the experimental observations. For the case of the "quinonoid" intermediate in tryptophan synthase, this approach demonstrated that the intermediate is better described as a carbanionic species with a deprotonated pyridine ring nitrogen – a structure that is fundamental to understanding reaction specificity in TS (34).

Here, NMR-assisted crystallography is used to characterize the TS α-aminoacrylate intermediate, (E(A-A); Fig.

1) a species that marks a divergent step in PLP catalysis, as only enzymes that perform β-elimination reactions generate this intermediate. For E(A-A), NMR-assisted crystallography is able to identify the protonation states of ionizable sites on the cofactor, substrates, and catalytic side chains, as well as the location and orientation of active site waters. From this, a detailed, three-dimensional picture of structure and reactivity emerges, highlighting βLys87 as the acid-base catalytic residue and delineating the reaction coordinate for the elimination of the substrate β-hydroxyl. Subsequent characterization of the Michaelis complex formed with the indole isostere, benzimidazole (BZI), shows BZI bound in the active site and poised for, but unable to initiate, the subsequent bond formation step. When modeled into the BZI position, indole is properly aligned for nucleophilic attack. The chemically-rich structure from NMR-assisted crystallography is key to understanding why BZI does not react, while indole does.

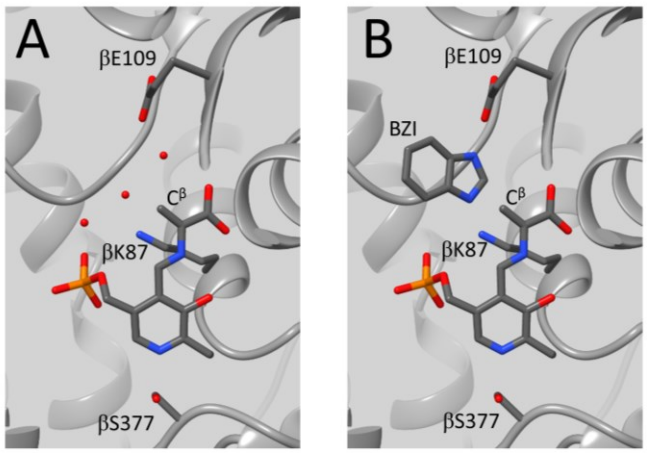

Fig. 2 The β-subunit active sites for E(A-A) and E(A-A)(BZI) from crystal structures 2J9X and 4HPX, respectively. (A) The E(A-A) intermediate shows 3 active site waters adjacent to the substrate with the central water forming close contacts to both the substrate C^{β} and the βLys87 ε-amino group. (B) The E(A-A)(BZI) complex shows BZI displacing the three waters, but otherwise inducing only small changes in the active site structure. Images rendered in UCSF Chimera (3).

Results and Discussion

X-ray Crystallography

X-ray crystal structures for the *St*TS E(A-A) and E(A-A)(BZI) complexes have been reported by our group (45) and others (46). Formation of E(A-A) is characterized by both the α- and β-subunits adopting closed conformations (2, 12, 45-48). The crystal structures for E(A-A) shows three crystallographic waters adjacent to the serine substrate in the β-subunit active site, forming a hydrogen bonded chain extending from the carboxylate of the catalytically essential βGlu109 (Fig. 2A). The position of the central water is particularly striking, as it forms close contacts to both the substrate C^{β} (d_{CO} = 3.2 Å) and the βLys87 ε-amino group (d_{NO} = 3.0 Å). This places the water close to the site that the substrate β-hydroxyl is expected to occupy before it is eliminated. The binding of BZI (Fig. 2B) displaces the waters and causes a small perturbation of the α-aminoacryloyl group. The binding also induces small movements of the βGlu109 carboxylate and the βLys87 ε-amino groups so that they are within hydrogen bonding distances of the BZI nitrogen atoms. These interactions and the close structural similarity of BZI to indole make the BZI complex a good mimic for the expected alignment of indole for nucleophilic attack at C^{β}. Absent in Fig. 2, however, are the hydrogen atoms, which are critical to identifying the hydrogen bond donors and acceptors and their mechanistic roles.

Solid-State NMR

SSNMR experiments were performed on microcrystalline protein samples prepared in close analogy to the single crystals used for X-ray crystallography. The single crystals were grown slowly using sitting drop vapor diffusion, while the microcrystals were formed rapidly using a batch approach in which the protein and crystallization buffer solutions were mixed to give the same final reagent concentrations as the crystal plate reservoirs. Microcrystals of TS prepared in this manner have been shown to maintain the same crystal habit as the larger crystals (49), giving high confidence that the NMR and X-ray data can be directly compared.

Both E(A-A) and E(A-A)(BZI) can be observed with SSNMR under conditions that favor the accumulation of the enzyme-bound species while the microcrystals remain catalytically active (49-51). SSNMR spectra of the reaction of L-Ser with microcrystalline TS to form E(A-A) are shown in Fig. 3. The signals in the cross-polarization magic-angle-spinning (CPMAS) spectra correspond to crystalline protein and bound substrate. The spectra were acquired with various combinations of ^{15}N and ^{13}C labels on the PLP cofactor, L-Ser substrate, and protein Lys ε-amino groups. With unlabeled substrate and protein (Fig. 3D), the spectra show only unresolved background signals from the protein, including the backbone amide nitrogens (~120 ppm) and backbone carbonyl (~170 ppm), aliphatic (~10-70 ppm), and aromatic (~110-160 ppm) carbons.

With the magnification of the isotopic enrichment (38), distinct resonances for the active site species become visible. The spectra of the sample prepared with ^{15}N and ^{13}C on the PLP cofactor (Fig. 3B,F) show a nitrogen resonance at 297.6 ppm and three additional carbon resonances at 17.5, 151.2, and 158.1 ppm that are assigned to the cofactor atoms N1, C2′, C2, and C3, respectively (atom labeling given in Fig. 3). The sample prepared using ^{13}C- and ^{15}N-L-Ser as a substrate (Fig. 3A,E,F,G) displays a nitrogen resonance at 286.7 ppm and additional carbon resonances at 170.9 ppm, 145.6 ppm, and 118.8 ppm that are assigned to the Schiff base nitrogen and carbons that derive from the serine C′, C^{α}, and C^{β}, respectively. The Schiff base nitrogen displays a significant temperature dependence of ~-0.14 ppm/K, while the PLP ring nitrogen shows no discernable temperature dependence (Fig. S6). The Schiff base nitrogen chemical shift tensor was measured under slow MAS conditions (Fig. S7), and the principal axis components, $\{\delta_{11}, \delta_{22}, \delta_{33}\}$ = {525 ±11, 305 ±10, 30 ±14} ppm, were extracted by fitting the intensity of the spinning sideband manifold (52).

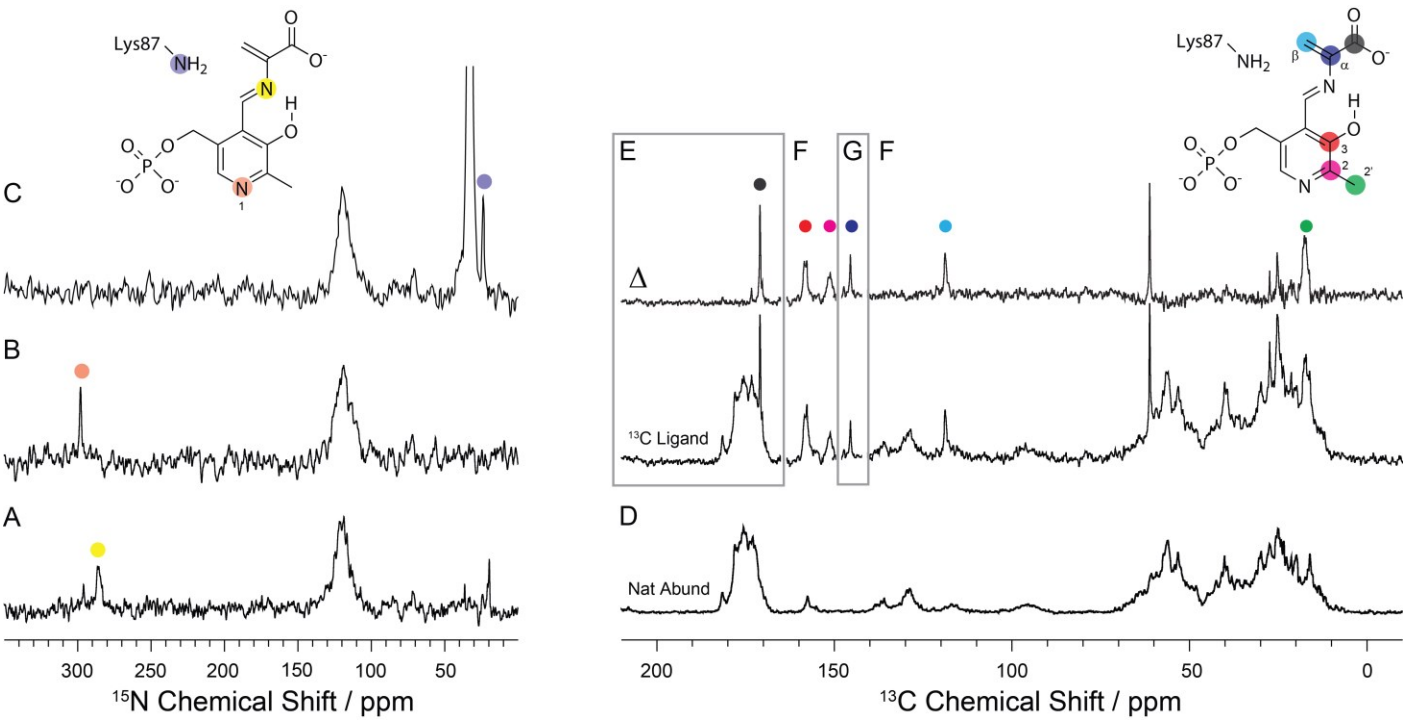

Fig. 3. ^{15}N and ^{13}C CPMAS SSNMR spectra of microcrystalline TS E(A-A) prepared with the following isotopic labeling: (A) ^{15}N-labeled on the substrate L-Ser; (B) ^{15}N-enriched on the PLP cofactor; (C) ^{15}N-enriched at protein lysine side chain ε-amino groups; (D) natural abundance isotopomer concentration; (E) ^{13}C-labeled on C′ of the L-Ser substrate; (F) ^{13}C,^{15}N-enriched on the PLP cofactor and C^{β} of the substrate L-Ser; and (G) ^{13}C-labeled on C^{α} of the substrate L-Ser. The top spectra in (E)-(G) are formed as the difference between the E(A-A) spectra with various cofactor/ligand isotopic labels and the same spectra acquired at natural abundance, emphasizing the resonances for the specific site labels. The large peak at 63.1 ppm is free serine. Spectra acquired at 9.4 T, -10 °C, and 8 kHz MAS as described in the *Materials and Methods*.

These shifts help establish several key elements of the chemical structure for E(A-A). At this point in the catalytic cycle, the serine substrate has lost its β-hydroxyl and there is a double bond between C^{α} and C^{β}, which is confirmed by their chemical shifts of 145.6 ppm and 118.8 ppm, respectively. Second, with a shift of 286.7 ppm, the Schiff base linkage is found to be neutral, which is further supported by the large span of its chemical shift tensor (53). This isotropic chemical shift, however, is below the limiting value for a fully neutral Schiff base, and the temperature dependence suggests tautomeric exchange involving transient protonation of this site (14, 34). At the same time, the PLP C2 and C3 shifts of 151.2 and 158.1 ppm indicate that the PLP phenolic oxygen is protonated (neutral) (34). The PLP nitrogen shift of 297.6 ppm also indicates a neutral pyridine ring N1.

The ^{15}N side chain chemical shift of βLys87 was measured on a TS sample in which all lysine residues were ^{15}N-labeled on the ε-amino group (ε-$^{15}NH_3$-Lys TS) as reported previously (50). In the initial resting state, E(Ain), this sample shows a peak at 202 ppm, corresponding to the protonated Schiff base linkage between βLys87 and the PLP cofactor (54). Upon addition of L-Ser, this resonance is lost and a new resonance at 24.2 ppm is observed (Fig. 3C), which is assigned to a neutral ε-amino group on βLys87.

The ^{31}P isotropic chemical shift and chemical shift tensor were also measured for the cofactor's phosphate group (Fig. S8). The phosphate chemical shift shows a characteristic response in going from the mono- to the dianionic charge state. The phosphate group's isotropic shift of 5.2 ppm and its shift tensor indicate that it is dianionic, in keeping with other TS intermediates (34, 54) and PLP-dependent enzymes (55).

Table 1. E(A-A) and E(A-A)(BZI) experimental and first-principles chemical shifts (ppm) for the phenolic (Phen) and protonated Schiff base (PSB) species and their two-site exchange with the following populations: E(A-A) 89.3% Phen,10.7% PSB; E(A-A)(BZI) 89.4% Phen, 10.6% PSB

E(A-A)	Atom	Phen	PSB	Two-Site	Expt
PLP	N1	302.9	303.3	303.0	297.6
	C2	148.7	159.1	149.8	151.2
	C2'	18.8	19.8	18.9	17.5
	C3	154.9	173.2	156.9	158.1
L-Ser	SB N	301.4	153.6	285.5	286.7
	Cα	144.4	133.1	143.2	145.6
	C'	171.2	168.7	171.0	170.9
	Cβ	123.3	121.3	123.0	118.8
	O1	262.1	261.4	262.0	257
	O2	302.4	294.3	301.5	289
βK87	Nζ	20.5	21.1	20.6	24.2
	red-χ^2	3.21	106.1	1.85	

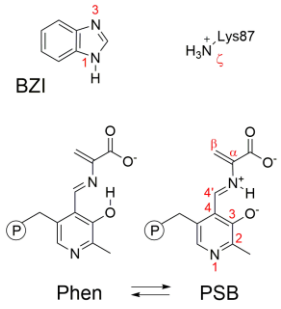

Two Site Exchange Model

E(A-A) (BZI)	Atom	Phen	PSB	Two-Site	Expt
PLP	N1	310.2	307.3	309.9	302.4
	C2	152.1	162.7	153.2	153.1
	C2'	19.4	20.7	19.6	18.2
	C3	155.2	174.0	157.2	158
L-Ser	SB N	307.6	152.0	291.2	292.3
	Cα	147.2	136.3	146.0	146
	C'	168.9	166.5	168.7	169.8
	Cβ	120.6	118.2	120.3	118.7
	O1	261.4	260.5	261.3	258
	O2	301.4	291.8	300.4	286
βK87	Nζ	35.6	36.4	35.6	35.6
BZI	N1	167.5	167.9	167.5	165.5
	N3	231.4	231.7	231.4	227.8
	red-χ^2	2.19	97.8	0.90	

Finally, the ^{17}O chemical shifts of the substrate carboxylate group were measured using ^{17}O quadrupole central transition (QCT) NMR in solution (56, 57) (Fig. S4). These were the only shifts measured for the intermediate in solution. ^{17}O NMR is not yet considered a standard high-resolution probe for biomolecular NMR, but QCT NMR takes advantage of the unique property of the NMR central transition to narrow as the size of the protein-substrate complex increases. We previously reported preliminary isotropic ^{17}O shifts for both E(A-A) and E(A-A)(BZI) (57). Here advantage is taken of additional measurements on the 35.2 T series connect hybrid magnet (58) at the National High Magnetic Field Laboratory to improve the accuracy of the extracted parameters (SI). The ^{17}O chemical shifts of 257 ppm and 289 ppm are consistent with an ionized carboxylate group. The upfield shifted signal is tentatively assigned to the oxygen hydrogen bonded to the side chain of βThr110, which forms the closest contact.

Chemical shifts for the E(A-A)(BZI) complex were measured analogously (Figs. S4-S10) and are summarized along with the E(A-A) shifts in Table 1. The spectra for E(A-A)(BZI) show two additional nitrogen resonances at 165.5 and 227.8 ppm that are assigned to N1 and N3 of bound BZI, respectively (atom labeling in Table 1). The spectra are otherwise similar to those for E(A-A) with one notable exception: the loss of the neutral amino resonance at 24.1 ppm and the appearance of an additional charged amino group at 35.6 ppm. The latter was assigned to the active site βLys87 based on ^{15}N{^{31}P}-rotational-echo double resonance (59) experiments that place it in close spatial proximity (<4 Å) to the phosphorus atom of the cofactor (Fig. S10). Thus, despite significant spectral overlap with the 26 other charged Lys side chains in TS, the catalytic active site residue can be uniquely identified. Similar strategies that make use of distinct chemical shifts, nuclides, and/or mixed labeling to assign and localize atoms within specific regions of proteins have been extensively demonstrated in solid-state NMR (60, 61).

First-Principles Calculations

While the preliminary chemical structures above shed significant light on the chemistry of the active site, they are incomplete in two important respects. First, they are absent in detailed three-dimensional structure. Second, the chemical shifts do not fully conform to the expected limiting shifts from model compound studies. To interpret the experimental chemical shifts and place the chemistry of the active site in full structural context, we turn to first-principles computational chemistry.

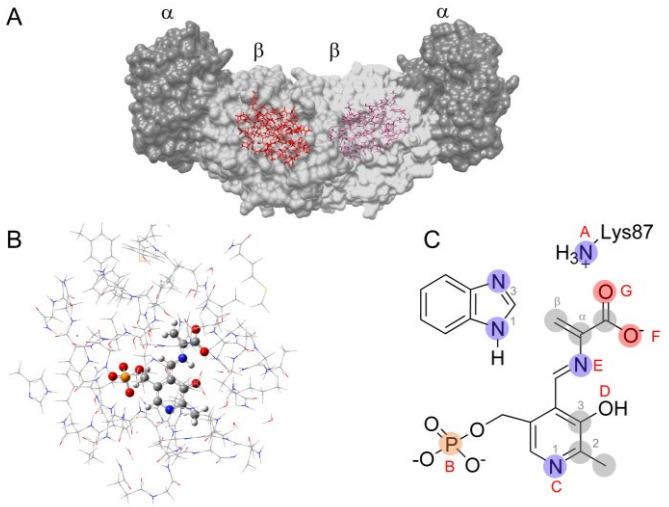

Fig. 4. Cluster model of the E(A-A) active site. (A) X-ray crystal structure of the TS $\alpha_2\beta_2$ heterodimer with the β-subunit active site in red. (B) Cluster model of the active site for first-principles geometry optimization and chemical shift calculations; protein side chains displayed in wireframe and cofactor and substrate in ball-and-stick. (C) Protonation sites on and near the cofactor/substrate complex: A: the βLys87 side chain; B: the PLP phosphate group; C: the PLP pyridine ring nitrogen; D: the PLP phenolic oxygen; E: the Schiff-base nitrogen; and F/G: the substrate carboxylate. Shaded nuclei indicate sites for which experimental NMR chemical shifts are reported.

The state-of-the-art for first-principles chemical shift calculations is advanced (31, 62-70), and extensive benchmarking and testing have shown that if the correct structure is known – down to the position of every atom – then the NMR chemical shifts can be predicted to better than 1.5 ppm RMSD for carbon, 4.3 ppm for nitrogen, and 7.5 ppm for oxygen (69, 70). This expected accuracy enables screening protocols to be established in which proposed structures can be evaluated and ranked for consistency with the experimental chemical shifts. Here this agreement is quantified using the reduced-χ^2 statistic, the squared deviation of the predicted and experimental chemical shifts weighted by the nuclide-dependent mean squared deviations (Eq. 4, *Materials and Methods*). The benchmark for a solved structure is taken as the identification of a single structure (or a fast-exchange equilibrium between closely related tautomers) that satisfies the 95% confidence limits of the reduced-χ^2. To fully distinguish proposed models typically requires 10-12 chemical shifts throughout the active site, supplemented by chemical shift tensor measurements and chemical shift temperature coefficients (34).

To limit bias and broadly consider various active site chemistries, a pool of candidate structures was generated by systematically varying the protonation states of the cofactor, substrates, and βLys87 ε-amino group (Fig. 4 and SI). The candidate structures were constructed directly as three-dimensional cluster models of the active site, built on the framework of the X-ray crystal structure, and included all residues and crystallographic waters within 7 Å of the substrate and cofactor. The atoms at the exterior of the cluster were fixed at their crystallographic locations, and quantum-mechanical, DFT-based geometry optimization and chemical shift calculations were performed. The clusters contained 703-706 atoms (Fig. 4B), a size for which the convergence and accuracy of the chemical shift calculations have been established (69).

35 initial models for E(A-A) and E(A-A)(BZI) were generated (Schemes S1 and S2), geometry optimized, and their chemical shifts predicted (Tables S1 and S2). The structures were ranked based on their agreement with the experimental chemical shifts (Fig. 5A,C). There is a clear differentiation of models for both E(A-A) and E(A-A)(BZI), but all candidate structures are found to fall outside of the reduced-χ^2 95% confidence limits, indicating that none reproduces the experimental chemical shifts with the expected accuracy. One of the largest discrepancies for all models occurs for the Schiff base nitrogen, where the closest predicted shifts are still greater than three standard errors from the experimental value.

Motivated by the temperature dependence of the Schiff base nitrogen, a two-site, fast-exchange equilibrium model was considered next in which the effective chemical shift is given as the population-weighted average of the individual shifts. To remain unbiased, all structures that differed by the position of a single hydrogen atom

were paired and their populations optimized for best overall agreement with the experimental data (Fig. 5B,D). Multiple exchange models are found to satisfy or come close to satisfying the 95% confidence limits. To differentiate these models, the predicted principal components of the Schiff base nitrogen chemical shift tensors were compared to the experimental values. The chemical shift tensor is extremely sensitive to dynamics, as it averages in both magnitude and orientation. For both E(A-A) and E(A-A)(BZI), only a single tautomeric exchange model is found to simultaneously satisfy both the isotropic and tensor chemical shift restraints, indicating that the benchmark for a solved structure has been reached.

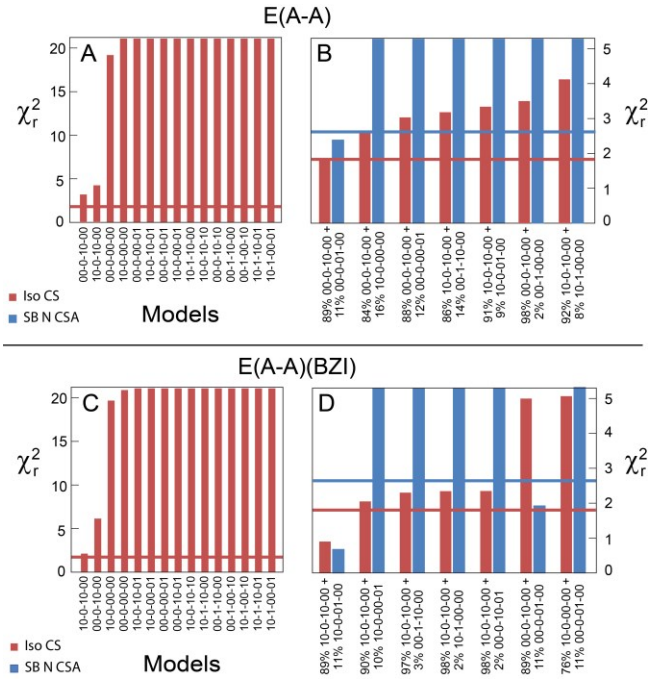

Fig. 5. Ranking of structural models based on agreement between the experimental and first principles chemical shifts as quantified by the reduced-χ^2 statistic. (A) The 15 best geometry-optimized active site models for the E(A-A) intermediate and (C) the E(A-A)(BZI) complex; structures and labeling given in Schemes S1 and S2. (B, D) Rankings of the 7 best fast-exchange equilibrium models comparing the experimental and first-principles isotropic chemical shifts (red) and Schiff base nitrogen tensor components (blue). 95% confidence limits are shown as the correspondingly colored horizontal bars.

For both E(A-A) and E(A-A)(BZI), the best-fit equilibrium is found to be between the phenolic (enolimine) (89%) and protonated Schiff base (ketoenamine) (11%) tautomers, with proton exchange across the internal hydrogen bond (Table 1, center inset). An analogous exchange was also found for the TS carbanionic intermediate (34) and appears to be a common feature in PLP-dependent enzymes (14). The only difference in protonation states between the E(A-A) and E(A-A)(BZI) structures is for the βLys87 ε-amino group: for E(A-A) it is neutral, while for E(A-A)(BZI) it is positively charged.

To further test the exchange model, the ^{15}N chemical shift of the Schiff base nitrogen was measured at 95 K under conditions of dynamic nuclear polarization (Fig. S6). At 95 K, the tautomeric equilibrium is expected to shift predominantly to the phenolic form, with less than 1% of the exchange partner present. This was confirmed experimentally, with chemical shifts of 301.4 ppm for E(A-A) and 302.1 ppm for E(A-A)(BZI) at 95 K, compared to the predicted shifts for the individual structures of 302.9 ppm and 310.2 ppm, respectively. Thus, both the major tautomers and the dynamic equilibrium of these intermediates can be established.

As a final assessment, the overall confidence in the identification of the experimental structure was quantified using Bayesian probability analysis following the approach of Engel et al. (71) as described in the SI. Taking into account both the isotropic and anisotropic chemical shift data, along with the observed temperature dependence of the Schiff base nitrogen, the proposed exchange model is found to be the most probable experimental structure with 88.5% confidence for E(A-A), and 99.6% confidence for E(A-A)(BZI). The decreased confidence for E(A-A) can be traced back to the lower overall agreement between the predicted and experimental shifts for the best-fit model as reflected in the reduced-χ^2. Dynamics of the waters adjacent to the substrate may explain why the overall agreement between theory and experiment is lower in this case.

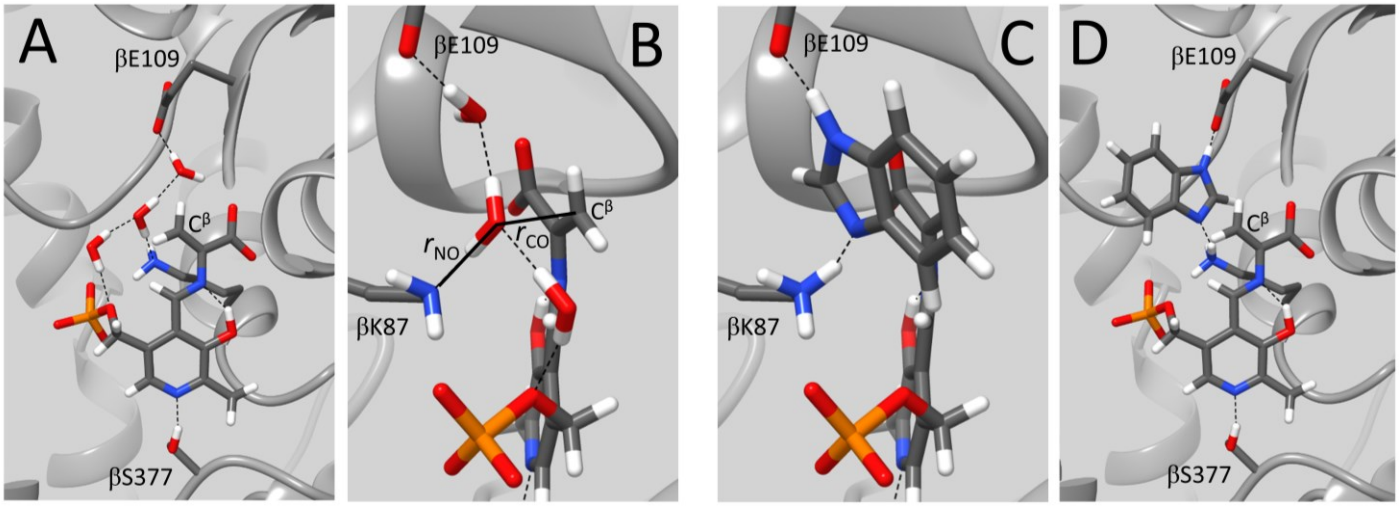

Fig. 6: Protonation states, hydrogen bonding interactions, and the placement and orientation of structural waters as revealed by NMR-assisted crystallography in the TS β-subunit active site. (A,B) the E(A-A) intermediate and (C,D) the E(A-A)(BZI) complex. For E(A-A), the position and orientation of the central water highlights the reaction coordinate for the loss of the serine β-hydroxyl and confirms βLys87 as the active site acid-base catalytic residue. The E(A-A)(BZI) complex shows BZI bound in the active site with hydrogen bonding interactions to βGlu109 and the charged ε-amino group of βLys87. BZI is poised for, but unable to initiate, the subsequent bond formation step. Images rendered in UCSF Chimera (3).

NMR-Assisted Crystallography

What emerges from the application of NMR-assisted crystallography to the α-aminoacrylate intermediate is a chemically-detailed view of the enzyme active site in which the locations of all atoms, including hydrogens, have been specified (Fig. 6). The quality of these structures can be judged by several metrics. First, the refined heavy atom positions are found to agree well with the original X-ray crystal coordinates, with RMSD of 0.077 Å for E(A-A) and 0.091 Å for E(A-A)(BZI). Second, the positional uncertainties in the structures from NMR-assisted crystallography can be estimated following the method of Hofstetter and Emsley (SI) (72). This approach correlates changes in the predicted shifts with displacements in the structural coordinates, defining a positional uncertainty that is consistent with the experimental shifts. Average positional RMSD of 0.11 Å for heavy atoms and 0.17 Å for hydrogen atoms are found for the cofactor and substrates in E(A-A) and E(A-A)(BZI). These positional uncertainties are similar in size to those found in organic molecular crystals (44, 72, 73), and are 6.5x smaller than the heavy atom uncertainties reported in the corresponding protein X-ray crystal structures. While preliminary, these results suggest that positional uncertainties in NMR crystallography are independent of molecular size, and that they will depend primarily on the nature and number of the measured NMR observables.

Chemically-Rich Crystal Structures and Mechanistic Implications

Perhaps most striking in the structure of the E(A-A) active site is the position of the central water immediately adjacent to the serine substrate C^{β} and oriented with one hydrogen pointing toward the ε-amino group of the catalytic βLys87 residue (Fig. 6B). This water is perfectly aligned for the reverse nucleophilic attack to regenerate E(C_1) and highlights the reaction coordinate for the loss of the serine β-hydroxyl. The interaction of this water with βLys87 and its proximity to the C^{β} carbon support the hypothesis that βLys87 is the acid catalyst that protonates the β-hydroxyl during C-O bond scission as E(C_1) is converted to E(A-A).

Critical examination of the crystal structures for E(A-A), however, shows that this central water is not consistently present. The electron density maps for 2J9X and 4HN4 (both with Cs^+ in the monovalent cation binding site) show significantly lower electron density for this water, and likely reflect occupancy less than 50% (Fig. S11). To explore this variation, two additional E(A-A) crystal structures for the NH_4^+ and Cs^+ forms were solved at 1.40 Å and 1.50 Å, respectively (PDBIDs 7MT4 and 7MT5). The diffraction data (Table S9) show

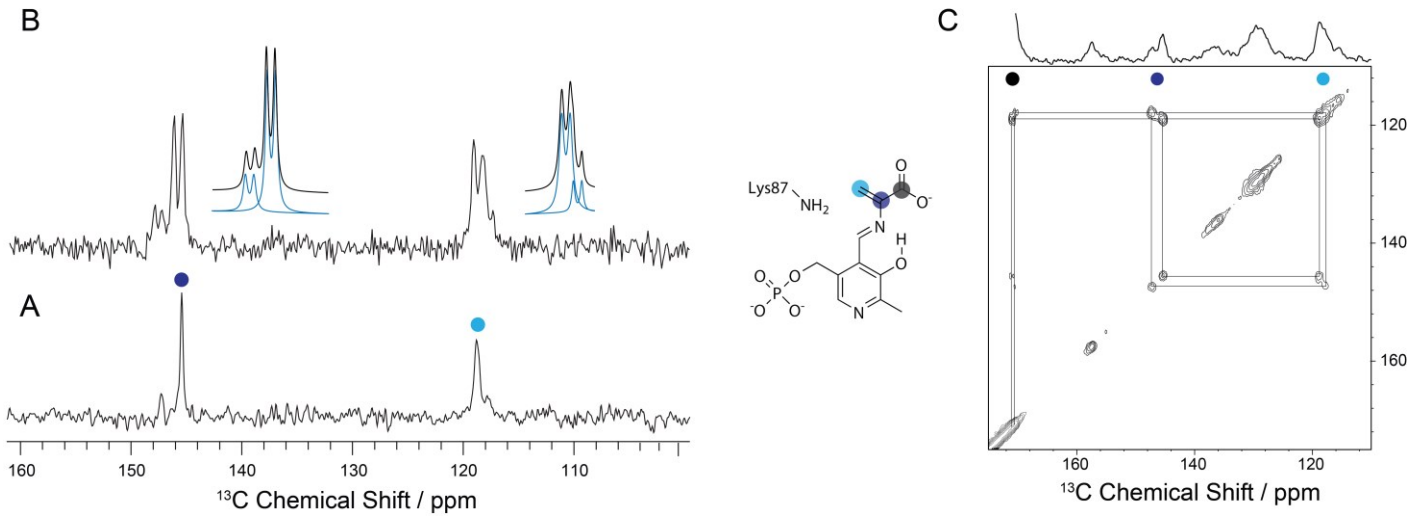

Fig. 7: ^{13}C SSNMR CPMAS spectra of the microcrystalline TS E(A-A) intermediate prepared with (A) a 50:50 mixture of singly-labeled 2-^{13}C-L-Ser and singly-labeled 3-^{13}C-L-Ser and (B) doubly labeled 2,3-$^{13}C_2$-L-Ser. For both, the natural abundance ^{13}C protein background has been subtracted as in Fig. 3. The C^{α} and C^{β} resonances show a minor peak that, along with the major peak, splits into a doublet upon incorporation of doubly labeled L-Ser substrate (deconvolution shown adjacent to the spectrum). (C) The 2D dipolar driven ^{13}C correlation spectrum of the E(A-A) formed with U-$^{13}C_3$-L-Ser displays distinct crosspeaks for the major and minor peaks, indicating that they belong to two independent E(A-A) species. The small chemical shift changes for the minor peaks correlate with the first-principles predicted shifts in the absence of the central water in E(A-A), consistent with the variable occupancy of this site across X-ray crystal structures. 1D spectra acquired as in Fig. 3; 2D Spectra acquired using CORD mixing (4) on a Bruker BioSolids CryoProbe™ (5) at 14.1 T, -10 °C (sample temp), and 8 kHz MAS as described in the Methods and Materials.

well-defined electron density for the central water in the NH_4^+ form, but an absence of this density in the Cs^+ structure (Fig. S11). Close inspection of the NMR data for E(A-A) indicates that each of the ^{13}C resonances of the bound serine is accompanied by slightly shifted (±1-2 ppm) minor species of ~20-30% intensity, while those for E(A-A)(BZI) show no such peaks. These resonances are most easily observed with single site ^{13}C serine labels (Fig. 7A) and display the same multiplet pattern as the major resonances upon incorporation of 2,3-$^{13}C_2$-L-Ser. The minor and major resonances also show distinct sets of cross-peaks (minor to minor, major to major) in the 2D dipolar-driven CORD correlation experiment (4), acquired with a CPMAS cryoprobe to improve sensitivity (Fig. 7C) (5). We hypothesize that the major and minor resonances belong to two independent E(A-A) species that derive from varying occupancy of the central water position across the macroscopic crystals. To test this, geometry-optimized active site models for the primary tautomers identified above were constructed in which the water nearest C^{β} was removed. Their predicted chemical shifts track the experimental chemical shifts of the minor species, and these secondary peaks are therefore tentatively assigned to a minor population in which the central water is no longer bound. Taken together, the SSNMR, X-ray, and computational results are consistent with this site being a weak binding site for water.

The E(A-A)(BZI) complex shows a similarly detailed view of the active site chemistry for the subsequent mechanistic step, nucleophilic addition at the substrate C^{β}. BZI is an isostere of indole and a potent inhibitor of the β-reaction (45, 74-76). The view from NMR-assisted crystallography (Fig. 6C,D) shows BZI bound in the active site, displacing the three waters, and poised for nucleophilic attack. Despite being more nucleophilic than indole, BZI does not react to form a covalent bond. A comparison to crystal structures for the carbanionic intermediate analogs formed with indoline and 2-aminophenol (34) makes it clear that BZI is bound to the same subsite. Thus, this intermediate analog appears to be poised close to the transition state between two reactive intermediates in the TS catalytic cycle.

That BZI is not a substrate for TS and does not covalently react with E(A-A) can be attributed to two important factors: the different nucleophilic reaction mechanisms of indole and BZI, and the tight packing and hydrogen bonding interactions within the indole subsite. The mechanisms of nucleophilic reaction for indole and BZI are fundamentally distinct, as BZI reacts via a nitrogen lone pair, and indole reacts via the pi system at C3 (74).

NMR-assisted crystallography identifies that it is the nucleophilic N3 that is adjacent to the substrate C^{β} in the E(A-A)(BZI) complex. Importantly, this structure shows that the BZI lone pair does not point toward the E(A-A) C^{β} p-orbital. The tight packing of atoms within the indole subsite, the hydrogen bond between N3 and the charged ε-amino group of βLys87, and the hydrogen bond between the βGlu109 carboxylate and N1 of BZI preclude rearrangement of BZI within the site to allow the reaction.

In contrast, when indole is modeled in place of BZI, the C3 carbon of the 5-membered ring is perfectly aligned to form the new C-C bond. The attacking p-orbital on indole points toward the electron deficient C^{β} carbon and is poised to make orbital overlap as the complex moves along the reaction coordinate to the sp^3 geometry of the product. At the same time, N1 of indole is positioned to hydrogen bond to the carboxylate of βGlu109, which stabilizes positive charge development on N1 as the transition state is approached. The C3 carbon of indole is relatively electron rich, but still requires assistance in the attack on C^{β}. The critical role played by βGlu109 can be seen in the βGlu109Asp mutation, which reduces the β reaction rate 27-fold (77). We posit that the E(A-A)(BZI) complex models how indole is bound to E(A-A) just prior to C-C bond formation.

Conclusions

The integrated application of SSNMR spectroscopy, X-ray crystallography, and first principles computational chemistry offers unprecedented, chemically-rich views of the TS E(A-A) and E(A-A)(BZI) active sites. Through the combined determination of heavy atom positions, the identification of protonation states, and the placement and orientation of active site waters, a clear picture of structure and reactivity emerges. The E(A-A) intermediate shows a central water that is well positioned for the reverse nucleophilic attack on C^{β}, with an orientation that points back to the active site acid-base catalytic residue, βLys87, highlighting the reaction coordinate for the elimination of the substrate β-hydroxyl. Both X-ray crystallography and SSNMR indicate variable occupancy for this site. Upon reaction of E(A-A) with BZI, these waters are displaced, and NMR-assisted crystallography shows BZI occupying the indole binding pocket, but unable to react. Here the protonation states complete the chemical picture for why BZI is unable to initiate the next step in the reaction: despite being a good nucleophile, BZI is held in the wrong orientation by hydrogen bonds to βGlu109 and the charged ε-amino group of βLys87.

NMR crystallography takes advantage of one of the well-established strengths of NMR spectroscopy – remarkable sensitivity to chemical structure and chemical dynamics. This is, we would argue, where NMR will continue to interface most strongly with the other tools of structural biology, including X-ray and neutron crystallography and cryo-EM. When combined with first-principles computational chemistry, these complementary techniques can build consistent, testable models of structure and reactivity in enzyme active sites. Importantly, this can be accomplished for samples near room temperature and under conditions of active catalysis.

Acknowledgements

The authors would like to thank M. Safo for providing the ePL Kinase K229Q mutant (78), and A. Hofstetter and L. Emsley for useful discussions regarding positional variances in NMR crystallography.

Research reported in this paper was supported by the United States National Science Foundation (CHE-1710671 to LJM, CHE-2002619 to RJH) and the US National Institutes of Health (GM097569 to LJM, MFD; GM137008 to LJM and TCM; NIH P41 GM122698 to JRL). Computations were performed using the computer clusters and data storage resources of the UCR HPCC, which were funded by grants from NSF (MRI-1429826) and NIH (S10OD016290). A portion of this work was performed at the National High Magnetic Field Laboratory, which is supported by National Science Foundation Cooperative Agreement Nos. DMR-1157490 and DMR-1644779 and the State of Florida. The gyrotron was purchased through an NSF MRI award, CHE-1229170, and the magnet and NMR console were purchased through NIH S10 OD018519. Development of the SCH magnet and NMR instrumentation were supported by NSF instrumentation grants (DMR-1039938 and DMR-0603042).

Materials and Methods

First principles calculations were performed using a cluster-based model of the active site as described previously (34). Tryptophan synthase was prepared by overexpression of *St*TS in *E. coli* (50, 54). Protein crystals of E(A-A) and E(A-A)(BZI) were prepared and structures solved following our earlier protocols (45, 79). SSNMR experiments followed our prior experimental design (34, 57), including DNP experiments at 95 K (80), and 2D correlation experiments performed on an MAS cryoprobe (5). ^{15}N-benzimidazole (BZI) was synthesized from $^{15}NH_4OH$ and 1-fluoro-2-nitrobenzene; 2,2′,3-$^{13}C_3$,^{15}N-PLP was prepared from U-$^{13}C_3$,^{15}N-Ala as previously detailed (54), while ^{15}N-PLP was prepared using a new synthetic strategy including enzymatic phosphorylation via the ePL Kinase K229Q mutant (78). Detailed Materials and Methods are included as part of the Supplemental Information.

References

1. E. W. Miles, Stereochemistry and mechanism of a new single-turnover, half-transamination reaction catalyzed by the tryptophan synthase $\alpha_2\beta_2$ complex. *Biochemistry* **26**, 597-603 (1987).
2. M. F. Dunn, Allosteric regulation of substrate channeling and catalysis in the tryptophan synthase bienzyme complex. *Arch. Biochem. Biophys.* **519**, 154-166 (2012).
3. E. F. Pettersen *et al.*, UCSF chimera - A visualization system for exploratory research and analysis. *J. Comput. Chem.* **25**, 1605-1612 (2004).
4. G. Hou, S. Yan, J. Trebosc, J. P. Amoureux, T. Polenova, Broadband homonuclear correlation spectroscopy driven by combined R2(n)(v) sequences under fast magic angle spinning for NMR structural analysis of organic and biological solids. *J Magn Reson* **232**, 18-30 (2013).
5. A. Hassan *et al.*, Sensitivity boosts by the CPMAS CryoProbe for challenging biological assemblies. *J Magn Reson* **311**, 106680 (2020).
6. C. Walsh, *Enzymatic Reaction Mechanisms* (W. H. Freeman and Company, San Francisco, 1979), pp. 978.
7. H. Hayashi, Pyridoxal Enzymes: Mechanistic Diversity and Uniformity. *J. Biochem.* **118**, 463-473 (1995).
8. R. Percudani, A. Peracchi, A genomic overview of pyridoxal-phosphate-dependent enzymes. *EMBO reports* **4**, 850-854 (2003).
9. M. D. Toney, Controlling reaction specificity in pyridoxal phosphate enzymes. *BBA - Proteins and Proteomics* **1814**, 1407-1418 (2011).
10. E. W. Miles, Tryptophan synthase: structure, function, and subunit interaction. *Adv. Enzymol. Relat. Areas Mol. Biol.* **49**, 127-186 (1979).
11. C. Yanofsky, I. P. Crawford, "Tryptophan Synthetase" in The Enzymes Third Edition, P. D. Boyer, Ed. (Academic Press, Inc., New York, NY, 1972), vol. 7, chap. 1, pp. 1-32.
12. M. F. Dunn, D. Niks, H. Ngo, T. R. Barends, I. Schlichting, Tryptophan synthase: the workings of a channeling nanomachine. *Trends Biochem. Sci* **33**, 254-264 (2008).
13. H. C. Dunathan, Conformation and Reaction Specificity in Pyridoxal Phosphate Enzymes. *Proc. Natl. Acad. Sci. USA* **55**, 712 (1966).
14. M. Chan-Huot *et al.*, NMR Studies of Protonation and Hydrogen Bond States of Internal Aldimines of Pyridoxal 5'-Phosphate Acid-Base in Alanine Racemase, Aspartate Aminotransferase, and Poly-L-lysine. *J. Am. Chem. Soc.* **135**, 18160-18175 (2013).
15. P. S. Langan *et al.*, Substrate binding induces conformational changes in a class A β-lactamase that prime it for catalysis. *ACS Catalysis* **8**, 2428-2437 (2018).
16. S. Dajnowicz *et al.*, Direct visualization of critical hydrogen atoms in a pyridoxal 5′-phosphate enzyme. *Nat. Commun.* **8**, 1-9 (2017).
17. K. M. Yip, N. Fischer, E. Paknia, A. Chari, H. Stark, Atomic-resolution protein structure determination by cryo-EM. *Nature* **587**, 157-161 (2020).
18. A. T. Petkova *et al.*, A structural model for Alzheimer's β-amyloid fibrils based on experimental constraints from solid state NMR. *Proc. Natl. Acad. Sci. U.S.A.* **99**, 16742-16747 (2002).
19. C. Luchinat, G. Parigi, E. Ravera, M. Rinaldelli, Solid-State NMR Crystallography through Paramagnetic Restraints.

J. Am. Chem. Soc. **134**, 5006-5009 (2012).
20. J.-P. Demers *et al.*, High-resolution structure of the Shigella type-III secretion needle by solid-state NMR and cryo-electron microscopy. *Nat. Commun.* **5**, 4976 (2014).
21. L. Sborgi *et al.*, Structure and assembly of the mouse ASC inflammasome by combined NMR spectroscopy and cryo-electron microscopy. *Proc. Natl. Acad. Sci. U.S.A.* **112**, 13237-13242 (2015).
22. R. Michalczyk *et al.*, Joint neutron crystallographic and NMR solution studies of Tyr residue ionization and hydrogen bonding: Implications for enzyme-mediated proton transfer. *Proc. Natl. Acad. Sci. U.S.A.* **112**, 5673-5678 (2015).
23. A. Carlon *et al.*, Improved Accuracy from Joint X-ray and NMR Refinement of a Protein–RNA Complex Structure. *J. Am. Chem. Soc.* **138**, 1601-1610 (2016).
24. L. Gremer *et al.*, Fibril structure of amyloid-β(1–42) by cryo–electron microscopy. *Science* **358**, 116-119 (2017).
25. J. R. Perilla *et al.*, CryoEM Structure Refinement by Integrating NMR Chemical Shifts with Molecular Dynamics Simulations. *J. Phys. Chem. B* **121**, 3853-3863 (2017).
26. K. Zhang *et al.*, Structure of the 30 kDa HIV-1 RNA Dimerization Signal by a Hybrid Cryo-EM, NMR, and Molecular Dynamics Approach. *Structure* **26**, 490-498.e493 (2018).
27. L. Cerofolini *et al.*, Characterization of PEGylated Asparaginase: New Opportunities from NMR Analysis of Large PEGylated Therapeutics. *Chemistry* **25**, 1984-1991 (2019).
28. D. F. Gauto *et al.*, Integrated NMR and cryo-EM atomic-resolution structure determination of a half-megadalton enzyme complex. *Nat. Commun.* **10**, 2697 (2019).
29. J. Felix *et al.*, Mechanism of the allosteric activation of the ClpP protease machinery by substrates and active-site inhibitors. *Sci. Adv.* **5**, eaaw3818 (2019).
30. S. Kosol *et al.*, Structural basis for chain release from the enacyloxin polyketide synthase. *Nat. Chem.* **11**, 913-923 (2019).
31. J. A. Gascon, E. M. Sproviero, V. S. Batista, QM/MM Study of the NMR Spectroscopy of the Retinyl Chromophore in Visual Rhodopsin. *J Chem Theory Comput* **1**, 674-685 (2005).
32. J. Lai *et al.*, X-ray and NMR crystallography in an enzyme active site: the indoline quinonoid intermediate in tryptophan synthase. *J. Am. Chem. Soc.* **133**, 4-7 (2011).
33. L. J. Mueller, M. F. Dunn, NMR crystallography of enzyme active sites: probing chemically detailed, three-dimensional structure in tryptophan synthase. *Acc. Chem. Res.* **46**, 2008-2017 (2013).
34. B. G. Caulkins *et al.*, NMR Crystallography of a Carbanionic Intermediate in Tryptophan Synthase: Chemical Structure, Tautomerization, and Reaction Specificity. *J. Am. Chem. Soc.* **138**, 15214-15226 (2016).
35. H. L. Zhang *et al.*, HIV-1 Capsid Function Is Regulated by Dynamics: Quantitative. Atomic-Resolution Insights by Integrating Magic-Angle-Spinning NMR, QM/MM, and MD. *J. Am. Chem. Soc.* **138**, 14066-14075 (2016).
36. H. Singh *et al.*, Fast Microsecond Dynamics of the Protein-Water Network in the Active Site of Human Carbonic Anhydrase II Studied by Solid-State NMR Spectroscopy. *J. Am. Chem. Soc.* **141**, 19276-19288 (2019).
37. A. Bertarello *et al.*, Picometer Resolution Structure of the Coordination Sphere in the Metal-Binding Site in a Metalloprotein by NMR. *J. Am. Chem. Soc.* **142**, 16757-16765 (2020).
38. J. C. Facelli, D. M. Grant, Determination of molecular symmetry in crystalline naphthalene using solid-state NMR. *Nature* **365**, 325-327 (1993).
39. M. Baias *et al.*, De novo determination of the crystal structure of a large drug molecule by crystal structure prediction-based powder NMR crystallography. *J. Am. Chem. Soc.* **135**, 17501-17507 (2013).
40. D. H. Brouwer *et al.*, A general protocol for determining the structures of molecularly ordered but noncrystalline silicate frameworks. *J. Am. Chem. Soc.* **135**, 5641-5655 (2013).
41. C. Martineau, NMR crystallography: Applications to inorganic materials. *Solid State Nucl. Magn. Reson.* **63**, 1-12 (2014).
42. D. Bryce, NMR crystallography: structure and properties of materials from solid-state nuclear magnetic resonance observables. *IUCrJ* **4**, 350-359 (2017).
43. P. Hodgkinson, NMR crystallography of molecular organics. *Prog. Nucl. Magn. Reson. Spectrosc.* **118-119**, 10-53 (2020).
44. M. Cordova *et al.*, Structure determination of an amorphous drug through large-scale NMR predictions. *Nat. Commun.* **12**, 2964 (2021).

45. D. Niks *et al.*, Allostery and substrate channeling in the tryptophan synthase bienzyme complex: evidence for two subunit conformations and four quaternary States. *Biochemistry* **52**, 6396-6411 (2013).
46. H. Ngo *et al.*, Allosteric regulation of substrate channeling in tryptophan synthase: modulation of the L-serine reaction in stage I of the beta-reaction by alpha-site ligands. *Biochemistry* **46**, 7740-7753 (2007).
47. M. A. Maria-Solano, J. Iglesias-Fernández, S. Osuna, Deciphering the allosterically driven conformational ensemble in tryptophan synthase evolution. *J. Am. Chem. Soc.* **141**, 13049-13056 (2019).
48. A. R. Buller *et al.*, Directed evolution mimics allosteric activation by stepwise tuning of the conformational ensemble. *J. Am. Chem. Soc.* **140**, 7256-7266 (2018).
49. S. A. Ahmed, C. C. Hyde, G. Thomas, E. W. Miles, Microcrystals of tryptophan synthase $\alpha_2\beta_2$ complex from Salmonella typhimurium are catalytically active. *Biochemistry* **26**, 5492-5498 (1987).
50. B. G. Caulkins *et al.*, Catalytic roles of βLys87 in tryptophan synthase: ^{15}N solid state NMR studies. *BBA - Proteins and Proteomics* **1854**, 1194-1199 (2015).
51. L. M. McDowell, M. S. Lee, J. Schaefer, K. S. Anderson, Observation of an Aminoacrylate Enzyme Intermediate in the Tryptophan Synthase Reaction by Solid-State NMR. *J. Am. Chem. Soc.* **117**, 12352-12353 (1995).
52. J. Herzfeld, A. E. Berger, Sideband intensities in NMR spectra of samples spinning at the magic angle. *J. Chem. Phys.* **73**, 6021-6030 (1980).
53. V. Copie, W. S. Faraci, C. T. Walsh, R. G. Griffin, Inhibition of alanine racemase by alanine phosphonate: detection of an imine linkage to pyridoxal 5'-phosphate in the enzyme-inhibitor complex by solid-state nitrogen-15 nuclear magnetic resonance. *Biochemistry* **27**, 4966-4970 (1988).
54. B. G. Caulkins *et al.*, Protonation states of the tryptophan synthase internal aldimine active site from solid-state NMR spectroscopy: direct observation of the protonated Schiff base linkage to pyridoxal-5'-phosphate. *J. Am. Chem. Soc.* **136**, 12824-12827 (2014).
55. K. D. Schnackerz, B. Andi, P. F. Cook, ^{31}P NMR spectroscopy senses the microenvironment of the 5'-phosphate group of enzyme-bound pyridoxal 5'-phosphate. *BBA - Proteins and Proteomics* **1814**, 1447-1458 (2011).
56. J. Zhu, G. Wu, Quadrupole central transition ^{17}O NMR spectroscopy of biological macromolecules in aqueous solution. *J. Am. Chem. Soc.* **133**, 920-932 (2011).
57. R. P. Young *et al.*, Solution-State ^{17}O Quadrupole Central-Transition NMR Spectroscopy in the Active Site of Tryptophan Synthase. *Angew. Chem. Int. Ed.* **55**, 1350-1354 (2016).
58. Z. Gan *et al.*, NMR spectroscopy up to 35.2 T using a series-connected hybrid magnet. *J. Magn. Reson.* **284**, 125-136 (2017).
59. T. Gullion, J. Schaefer, Rotational-Echo Double-Resonance NMR. *J. Magn. Reson.* **81**, 196-200 (1989).
60. A. K. Schütz, Solid-state NMR approaches to investigate large enzymes in complex with substrates and inhibitors. *Biochem. Soc. Trans.* **49**, 131-144 (2020).
61. J. Kraus, S. Sarkar, C. M. Quinn, T. Polenova, "Solid-state NMR spectroscopy of microcrystalline proteins" in Annual Reports on NMR Spectroscopy, G. A. Webb, Ed. (Academic Press, 2021), vol. 102, pp. 81-151.
62. A. C. de Dios, J. G. Pearson, E. Oldfield, Secondary and tertiary structural effects on protein NMR chemical shifts: an ab initio approach. *Science* **260**, 1491-1496 (1993).
63. Q. Cui, M. Karplus, Molecular Properties from Combined QM/MM Methods. 2. Chemical Shifts in Large Molecules. *J. Phys. Chem. B* **104**, 3721-3743 (2000).
64. L. B. Casabianca, A. C. de Dios, Ab initio calculations of NMR chemical shifts. *J. Chem. Phys.* **128**, 052201 (2008).
65. J. C. Facelli, Chemical shift tensors: theory and application to molecular structural problems. *Prog. Nucl. Magn. Reson. Spectrosc.* **58**, 176-201 (2011).
66. T. E. Exner, A. Frank, I. Onila, H. M. Möller, Toward the Quantum Chemical Calculation of NMR Chemical Shifts of Proteins. 3. Conformational Sampling and Explicit Solvents Model. *J. Chem. Theory Comput.* **8**, 4818-4827 (2012).
67. J. Swails, T. Zhu, X. He, D. A. Case, AFNMR: automated fragmentation quantum mechanical calculation of NMR chemical shifts for biomolecules. *J. Biomol. NMR* **63**, 125-139 (2015).
68. S. K. Chandy, B. Thapa, K. Raghavachari, Accurate and cost-effective NMR chemical shift predictions for proteins using a molecules-in-molecules fragmentation-based method. *Phys. Chem. Chem. Phys.* **22**, 27781-27799 (2020).
69. J. D. Hartman, T. J. Neubauer, B. G. Caulkins, L. J. Mueller, G. J. Beran, Converging nuclear magnetic shielding calculations with respect to basis and system size in protein systems. *J. Biomol. NMR* **62**, 327-340 (2015).
70. J. D. Hartman, R. A. Kudla, G. M. Day, L. J. Mueller, G. J. Beran, Benchmark fragment-based ^{1}H, ^{13}C, ^{15}N and ^{17}O

chemical shift predictions in molecular crystals. *Phys. Chem. Chem. Phys.* **18**, 21686-21709 (2016).
71. E. A. Engel *et al.*, A Bayesian approach to NMR crystal structure determination. *Phys. Chem. Chem. Phys.* **21**, 23385-23400 (2019).
72. A. Hofstetter, L. Emsley, Positional Variance in NMR Crystallography. *J. Am. Chem. Soc.* **139**, 2573-2576 (2017).
73. L. Wang, F. J. Uribe-Romo, L. J. Mueller, J. K. Harper, Predicting anisotropic thermal displacements for hydrogens from solid-state NMR: a study on hydrogen bonding in polymorphs of palmitic acid. *Phys. Chem. Chem. Phys.* **20**, 8475-8487 (2018).
74. M. Roy, S. Keblawi, M. F. Dunn, Stereoelectronic control of bond formation in Escherichia coli tryptophan synthase: substrate specificity and enzymatic synthesis of the novel amino acid dihydroisotryptophan. *Biochemistry* **27**, 6698-6704 (1988).
75. M. F. Dunn *et al.*, The tryptophan synthase bienzyme complex transfers indole between the alpha- and beta-sites via a 25-30 Å long tunnel. *Biochemistry* **29**, 8598-8607 (1990).
76. R. M. Harris, H. Ngo, M. F. Dunn, Synergistic effects on escape of a ligand from the closed tryptophan synthase bienzyme complex. *Biochemistry* **44**, 16886-16895 (2005).
77. P. S. Brzovic, A. M. Kayastha, E. W. Miles, M. F. Dunn, Substitution of glutamic acid 109 by aspartic acid alters the substrate specificity and catalytic activity of the β-subunit in the tryptophan synthase bienzyme complex from Salmonella typhimurium. *Biochemistry* **31**, 1180-1190 (1992).
78. M. S. Ghatge *et al.*, Pyridoxal 5'-Phosphate Is a Slow Tight Binding Inhibitor of E. coli Pyridoxal Kinase. *PLOS ONE* **7**, e41680 (2012).
79. E. Hilario *et al.*, Visualizing the tunnel in tryptophan synthase with crystallography: Insights into a selective filter for accommodating indole and rejecting water. *BBA - Proteins and Proteomics* **1864**, 268-279 (2016).
80. X. Wang *et al.*, Direct dynamic nuclear polarization of ^{15}N and ^{13}C spins at 14.1 T using a trityl radical and magic angle spinning. *Solid State Nucl. Magn. Reson.* **100**, 85-91 (2019).